AIP | Physics of Fluids

Modification of vortex dynamics and transport properties of transitional axisymmetric jets using zero-net-mass-flux actuation

Asim Önder and Johan Meyers

Citation: Physics of Fluids (1994-present) **26**, 075103 (2014); doi: 10.1063/1.4890242
View online: http://dx.doi.org/10.1063/1.4890242
View Table of Contents: http://scitation.aip.org/content/aip/journal/pof2/26/7?ver=pdfcov
Published by the AIP Publishing

PHYSICS OF FLUIDS **26**, 075103 (2014)

Modification of vortex dynamics and transport properties of transitional axisymmetric jets using zero-net-mass-flux actuation

Asim Önder and Johan Meyers[a)]
Department of Mechanical Engineering, KU Leuven, Celestijnenlaan 300A, B3001 Leuven, Belgium

(Received 16 May 2014; accepted 26 June 2014; published online 24 July 2014)

We study the near field of a zero-net-mass-flux (ZNMF) actuated round jet using direct numerical simulations. The Reynolds number of the jet $Re_D = 2000$ and three ZNMF actuators are used, evenly distributed over a circle, and directed towards the main jet. The actuators are triggered in phase, and have a relatively low momentum coefficient of $C_\mu = 0.0049$ each. We study four different control frequencies with Strouhal numbers ranging from $St_D = 0.165$ to $St_D = 1.32$; next to that, also two uncontrolled baseline cases are included in the study. We find that this type of ZNMF actuation leads to strong deformations of the near-field jet region that are very similar to those observed for non-circular jets. At the end of the jet's potential core ($x/D = 5$), the jet-column cross section is deformed into a hexagram-like geometry that results from strong modifications of the vortex structures. Two mechanisms lead to these modifications, i.e., (i) self-deformation of the jet's primary vortex rings started by distortions in their azimuthal curvature by the actuation, and (ii) production of side jets by the development and subsequent detachment of secondary streamwise vortex pairs. Further downstream ($x/D = 10$), the jet transforms into a triangular pattern, as the sharp corner regions of the hexagram entrain fluid and spread. We further investigate the global characteristics of the actuated jets. In particular when using the jet preferred frequency, i.e., $St_D = 0.33$, parameters such as entrainment, centerline decay rate, and mean turbulent kinetic energy are significantly increased. Furthermore, high frequency actuation, i.e., $St_D = 1.32$, is found to suppress the mechanisms leading to large scale structure growth and turbulent kinetic energy production. The simulations further include a passive scalar equation, and passive scalar mixing is also quantified and visualized. [http://dx.doi.org/10.1063/1.4890242]

I. INTRODUCTION

Axisymmetric jet flow is a prime example of a fundamental flow that received considerable technological and scientific attention. It is well known that the flow field is completely determined by upstream conditions.[1] Especially the near field development ($x < 10D$) is very sensitive to the inlet profile and its perturbations.[2] Due to the convective nature of the axisymmetric jet, modifications in the near field can also be carried out to the intermediate and far field[3] where nonlinear dynamics are the dominant mechanism. This sensitivity of jet flow triggered numerous control efforts over the years.

Control designs aim at the manipulation of coherent vortical features, and their interactions and eventual breakdown to finer scales of turbulence. In jet flows these structures are induced by instability mechanisms of the mean inlet jet profile. A primary instability in naturally evolving round jets is the Kelvin-Helmholtz (KH) instability of the initial shear layer where the growth of initial

[a)]Electronic mail: johan.meyers@mech.kuleuven.be

disturbances results in shedding of toroidal vortex rings. Consecutive KH rings can merge by mutual induction,[4] lose their axisymmetry, and give rise to secondary instabilities oriented in streamwise direction as braid region vortices.[5] In an uncontrolled jet these events occur randomly. Therefore, the main strategy in jet flow control is controlling the evolution of primary and secondary instabilities by imposing axial and azimuthal perturbations in an organized fashion.

Passive steady controls are based on introducing azimuthal perturbations by modifying inlet nozzle designs. Elliptic, triangular and rectangular nozzles,[6] mounted vortex generators and tabs,[7] and lobed nozzles[8] are common examples enhancing mass entrainment rate. Here broken axisymmetry of the inlet geometry causes variations in the azimuthal curvature of primary rings which lead to self-induced Biot-Savart deformations[9] and eventually the development of streamwise vortex structures. These are known for their ability to promote entrainment and bulk mixing in the near field of the jet.[10] The complex interactions of streamwise and azimuthal vortices give also rise to fine-scale developments when the jet convects further downstream and increases mixing in the local molecular sense. In contrast to these nozzle designs that focus on augmentation of turbulence and mixing, chevron nozzles suppress the turbulence and spreading of the jet and are therefore favourable to reduce acoustic emissions. In chevron jets counter-rotating streamwise vortex pairs dominate the near field dynamics, and growth of azimuthal structures is delayed.[5] Similar effects can also be achieved by the use of micro jets.[11]

Active controls mostly impose periodic excitations to trigger the instability modes of jets. In this way, axisymmetric excitations can induce dramatic changes, in which vortex rings are synchronized and shed with the forcing frequency. The most amplified frequency is called the jet preferred mode. Its value was first determined by Ref. 12 at $St_D = fD/U_J = 0.3$ and can be linked to the shear layer mode frequency.[13,14] Forcing with this natural jet frequency can lead to surprising secondary instabilities also known as "side jets." On transverse views they appear as secondary mini-jets ejected radially away from jet core giving the jet star-like patterns. They were first observed in experiments with low-density jets[15] where self-sustained global oscillations regularize and synchronize primary ring structures to the natural frequency mode. The same phenomenon can also be observed for regular homogenous jets using strong axial forcing.[16,17] The key element here is the synchronization of vortex rings so that their strength and size is promoted. Then, appearance of lobes on these rings due to azimuthal instabilities induces a positive strain in the braid region giving rise to streamwise vortex filaments. Side jets are formed by these counter-rotating vortex pairs initially oriented in axial direction but soon propelling away from the jet centreline by their own induction and causing anomalous spreading on streamwise planes. These long-lived structures are also responsible for enhanced mixing and entrainment.[18]

One of the most popular time-periodic fluidic actuators is the so-called synthetic jet or zero-net-mass-flux (ZNMF) actuator.[19] These actuators are quite attractive in the sense that they do not require an external fluid source, and work simply with the ambient fluid. Due to their oscillatory nature, there is no net mass addition to the main flow. Nevertheless, ZNMF actuators are capable of transferring a net momentum. Parallel allocation of a ZNMF actuator with respect to the main jet can cause vectoring of the main jet if the control frequency is orders of magnitude higher than main jet instability frequencies.[20] If a ZNMF actuator is pointed to the main jet centreline, the effect is more complex due to direct impact. The synthetic jet can penetrate into the primary jet and break down its azimuthal symmetry. Depending on the momentum coefficient and therefore the degree of penetration this may initiate vortex induction mechanisms for increased entrainment such as in non-circular jets or turbulence suppression mechanisms as in chevron jets. These effects also depend on actuation frequency which allows manipulating global scale modes of the jet. Having a great flexibility to configure actuation frequency and momentum, ZNMF actuators have the capacity to become a versatile and powerful jet control device.

Despite their strong potential, ZNMF actuators in jet flow control remain relatively unexplored. Tamburello and Amitay[21] investigated the interaction of a single synthetic jet with an axisymmetric jet with $Re_D = 6600$ using various momentum coefficients ($0.005 < C_\mu < 0.16$) and frequencies ($0.16 < St_D < 0.48$). Mounting the ZNMF actuator $1.25D$ away from the jet centreline they observed the largest effect for $St_D = 0.32$ in low C_μ excitation, and no sensitivity to the actuation frequency for high C_μ. They also identified counter-rotating streamwise vortices

resulting from jet penetration and showed that their size and strength increased with momentum coefficient.

To our knowledge, there have not been any numerical studies for ZNMF actuated round jets that carefully visualize the characteristics of three-dimensional vortex topology, and elucidate mechanisms for their evolution. In the present study, the motivation is to numerically investigate these typical flow patterns and their effect on key jet parameters and to make connections to the bulk literature of jet flow. To this end, we explore the effect of multiple ZNMF actuation on the near field of a transitional axisymmetric jet with $Re_D = 2000$ using direct numerical simulation (DNS). A passive scalar-transport equation is also included in the DNS study. The momentum coefficients of the actuators are fixed to a low value (i.e., $C_\mu = 0.0049$). The primary objective is analysing the effect of excitation frequencies.

We find that actuation in preferred mode regime leads to a strong production of side jets, which dominates the dynamics of the jet, and leads to star-shaped patterns in the jet transverse sections. We discuss the driving mechanisms for side jets and present the role of streamwise vortex filaments by revisiting earlier numerical simulations in a temporal setting.[22,23] Thus, the present work is a novel numerical attempt to investigate this intricate vortex dynamics in a realistic spatially developing setting. In addition, we find that actuation with high frequencies distinctively reduces structure growth and jet spreading. We elaborate also this suppression mechanism.

We further find that dramatic changes in the structure of the dominant streamwise and axisymmetric vortices lead to global changes in the flow that have a direct influence on centreline decay rate, evolution of centreline fluctuating energy, and entrainment in the jet transition region. We also study mixing efficiency by investigating statistical averages of the passive scalar evolution, and the passive scalar transport tubes. The latter are equivalent to the heatline method proposed by Kimura and Bejan,[24] and the concept of momentum and energy transport tubes later proposed by Meyers and Meneveau.[25]

The structure of this paper is as follows. First, the computational details and flow configuration are described in Sec. II. Then we will analyse the features of the instantaneous flow field in Sec. III. Subsequently, first and second order statistics are discussed in Sec. IV, and the passive scalar evolution and scalar transport tubes are presented. Finally, conclusions are presented in Sec. V.

II. METHODOLOGY AND COMPUTATIONAL SET-UP

In this section, we define the flow configuration in Sec. II A. Subsequently, computational details are presented in Sec. II B, followed by a grid-assessment study in Sec. II C.

A. Flow configuration

We consider a jet discharged into the free motionless ambient fluid through an axisymmetric orifice with a diameter D. The orifice is surrounded by solid walls. In addition, the jet contains a scalar quantity which will be used in our mixing analysis. The governing equations are the full incompressible Navier-Stokes equations normalized by jet diameter D, and outlet velocity U_J, i.e.,

$$\frac{\partial u_i}{\partial t} + \frac{\partial u_i u_j}{\partial x_i} = -\frac{\partial p}{\partial x_i} + \frac{1}{Re_D}\frac{\partial^2 u_i}{\partial x_j \partial x_j}, \tag{1}$$

$$\frac{\partial u_i}{\partial x_i} = 0, \tag{2}$$

and a passive scalar transport equation

$$\frac{\partial c}{\partial t} + \frac{\partial u_i c}{\partial x_i} = \frac{1}{Re_D Sc}\frac{\partial^2 c}{\partial x_j \partial x_j}, \tag{3}$$

where u_i are the fluid velocity components, c is the passive scalar, Re_D denotes the Reynolds number based on orifice diameter and jet outlet velocity, and Sc denotes the Schmidt number. All the cases

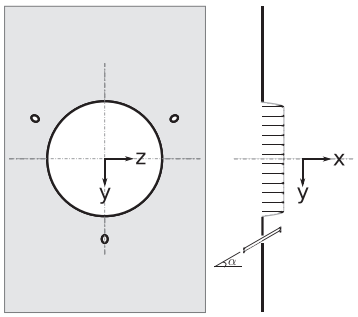

FIG. 1. Configuration of the actuators.

considered in this work have a Reynolds number of $Re_D = 2000$ and a Schmidt number $Sc = 1.0$. At this Reynolds number the flow is initially laminar and becomes turbulent downstream. Direct numerical simulations are carried out without any further turbulence-modelling assumptions.

The inflow profile is essential in the description of the flow as it plays a crucial role in the near field flow development. In the present study, we specify a uniform velocity U_J in the core region of the jet, and and laminar Blasius profile in the vicinity of the wall similar to previous numerical work.[2] The associated inlet momentum thickness, defined as

$$\theta_0 = \frac{2}{D}\int_0^{D/2} \frac{U_x(r)}{U_J}\left(1 - \frac{U_x(r)}{U_J}\right) r \, \mathrm{d}r, \tag{4}$$

corresponds to $D/2\theta_0 \approx 88$ in our study.

For the control of the main jet we employ three ZNMF actuators distributed evenly in circumferential direction and placed $0.625D$ away from the jet centreline, and inclined at an angle of $\alpha = 30^\circ$ with the jet centreline (cf. Figure 1). The ZNMF actuators and cavities are not represented in full detail, but instead, the actuators are modelled as an oscillating inlet-velocity boundary condition on the wall, with

$$u_a = U_a \sin(2.0\pi f_a t). \tag{5}$$

This simple control model is inspired by the experimental phase locked velocity measurements on the centreline of a synthetic jet with a step.[19] The boundary condition is imposed on an elliptic actuation surface, i.e., resulting from the $\alpha = 30^\circ$ inclination of the ZNMF jets (cf. Figure 1). The individual actuators have a momentum coefficient of $C_\mu = 0.0049$ and a ratio between actuation velocity to main jet velocity of $U_a/U_J = 1$. All the controls are in phase, manipulating the axisymmetric modes of the main jet.

The different simulation cases studied in this work are listed in Table I. First of all, two baseline cases without any control are included. In fact, in absence of any other perturbations, we observed for uncontrolled simulations a rather late transition to turbulence. Since all controlled cases in this work display an early transition, the two baseline cases contain additional random perturbations on the jet inlet profile. In the first baseline case (*B1*) these have an amplitude of $u'_J = 0.015U_J$ (with u'_J the rms value), while in the other baseline case (*B2*) a higher amplitude of $u'_J = 0.075U_J$ is used.

TABLE I. Nomenclature and control parameters of investigated cases. (St_D): actuation frequency, (u'_J/U_J): background turbulence level, (C_μ): momentum coefficient for individual actuators.

Cases	*B1*	*B2*	*C0.5*	*C1*	*C2*	*C4*
St_D	0	0	0.165	0.33	0.66	1.32
u'_J/U_J	0.015	0.075	0.0015	0.0015	0.0015	0.0015
C_μ	0	0	0.0049	0.0049	0.0049	0.0049

We further assume that the Strouhal number ($St = fD/U_J$) of the jet preferred mode $St_{pm} = 0.33$—for Case *B2* we observed a peak in the velocity spectra at this Strouhal number. This value is consistent with the experimental results in Ref. 14 considering our initial boundary layer thickness with $D/2\theta_0 \approx 88$. Four control cases are then considered (cf. Table I), i.e., with control frequencies of $St = 0.165$, $St = 0.33$, $St = 0.66$, and $St = 1.32$, or ranging from one half (*C0.5*) up to four times (*C4*) the Strouhal number of the preferred mode. In the controlled cases the perturbation level on the baseline jet is reduced to $u'_J = 0.0015U_J$, in order to prevent that the uncontrolled excitation by white noise becomes more dominant for the flow development than the ZNMF actuation with only a momentum coefficient of $C_\mu = 0.0049$.

B. Computational details

The open-source C++ library OpenFOAM[26] is employed in this study (using the v2.1.x distribution). In OpenFOAM the equations are discretized in space using a collocated finite volume method where all the variables are stored at the centroids of the grid elements. In our simulations, the face values for the calculation of convective and diffusive terms are approximated using linear interpolation. The flux velocities on faces are modified using Rhie–Chow interpolation to prevent velocity-pressure decoupling. The nonlinear convective term is linearized by employing a second order extrapolation in time for the velocity flux. Temporal discretization is done by using a semi-implicit Crank–Nicolson scheme. All the terms are fully implicit except the linearized semi-implicit convective term.

An incremental projection scheme[27] is implemented to replace the costly iterative PISO algorithm in OpenFOAM. The coupled system of momentum and continuity equations are segregated with this scheme which results in an additional second order segregation error in time. Hence, the order of accuracy of the segregation is consistent with the employed second-order temporal discretization. Following the projection scheme, during each time step a linear system of convection-diffusion like equations for each velocity component has to be solved. This is done by using the biconjugate gradient iterative solver with a diagonal incomplete LU preconditioner up to a solution tolerance of 10^{-9}. The second more expensive step of the projection scheme requires solving a discretized Poisson equation for the pressure which is achieved by using a conjugate gradient solver with a geometric-algebraic multigrid preconditioner up to a tolerance of 10^{-10}.

A cylindrical computational domain is selected which extends $L = 16D$ in axial direction and $R = 8D$ in radial direction. A multiblock-structured grid using hexahedral elements with a square-shaped central block and an O-grid formed of surrounding blocks is constructed (cf. Fig. 2). The grid

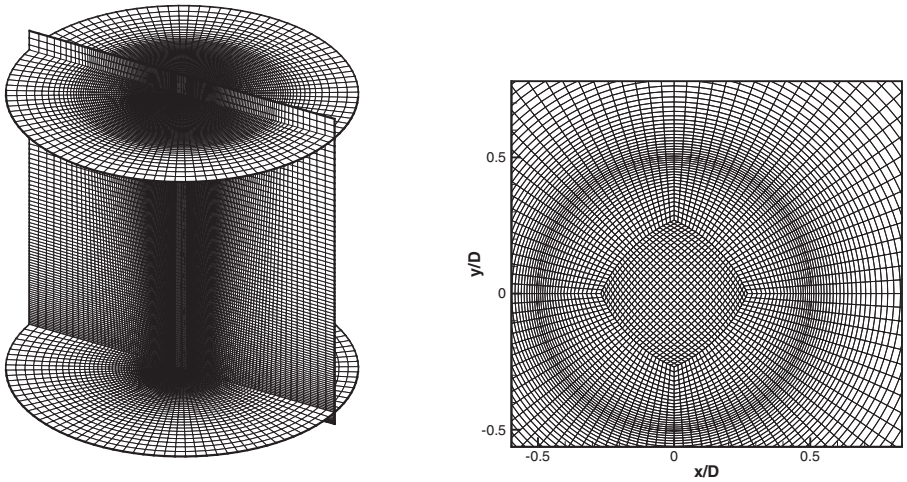

(a) (b)

FIG. 2. Computational grid. Every fifth line is shown. (a) Slices of streamwise and spanwise cross-sections, $z = 15.5D$. (b) Zoom on a streamwise cross-section at $x = 0$ close to the jet axis.

resolution is fixed to $130(x) \times 130(y) \times 475(z)$ elements for the core region and $470(r) \times 520(\theta) \times 475(z)$ elements for the O-grid region, totalling to around 125×10^6 elements. Close to the jet exit, the grid elements are clustered in the jet core region, especially in the shear layer. This cluster region expands radially moving downstream following the expected jet spreading. In order to represent the synthetic jet–main jet interaction, a relatively higher circumferential resolution is used compared to the uncontrolled round jet simulations. Also in the streamwise direction refinements are applied in the vicinity of the wall to resolve the oscillatory actuation dynamics.

The boundary conditions at lateral and outflow boundaries correspond, respectively, to $\partial u_i/\partial r = 0$ and $\partial u_i/\partial x = 0$. No inflow is allowed on the outflow boundary. The ZNMF inlet boundary (cf. Eq. (5)) is treated in a special way. Instead of body-fitting the mesh to the elliptic ZNMF openings, we project the effect of actuation on the DNS grid using a two-dimensional axisymmetric convolution filter. The actuators are located in regions discretized with an O-grid, where grid lines are aligned with a cylindrical coordinate system having the jet centreline as reference axis. Applying filtering in this coordinate system the filtered actuation velocity at the center of a face element corresponds to

$$\tilde{\boldsymbol{u}}_a(r_h, \theta_h) = \iint \boldsymbol{u}_a(r, \theta)\, G(r - r_h)\, G(\theta - \theta_h)\, r_h \,\mathrm{d}\theta \mathrm{d}r, \tag{6}$$

where r_h, θ_h are the radial distance and angular position of the cell center, respectively, and $G(r)$ is the filter kernel $G(r) = (6/\pi\,\Delta^2)^{1/2}\exp(-6r^2/\Delta^2)$ with filter width $\Delta = 1.5h_r$ (where h_r is the cell size in radial direction).

In OpenFOAM, parallelism is achieved by grid partitioning. The simulations are run on the supercomputer of Flemish Supercomputer Center (VSC) that is equipped with a total of 8448 computer cores with Intel Sandy Bridge microprocessor technology, and an FDR Infiniband Mellanox communication network. We observed in our scaling studies that the maximum number of processors remains under $p \approx 400$ if we want to keep parallel efficiency above 0.8. To circumvent this bottleneck, we use a method to improve the efficiency of parallelism by using an optimal combination of ensemble averaging and grid partitioning.[28] For turbulent flow systems that are statistically stationary, simulations are first run for some period of time T_i during which the flow starts from an initial condition, and subsequently settles into a statistical equilibrium. Afterwards, statistics are collected over a period of time T_s. If $T_i \ll T_s$, as is the case for our turbulent jet, we can efficiently approximate the statistical moments by combining ensemble averaging with time averaging, i.e.,

$$\langle \boldsymbol{u}(\boldsymbol{x}) \rangle \approx \frac{1}{R} \sum_{r=1}^{R} \frac{R}{T_S} \int_{t_0}^{t_0 + T_S/R} \boldsymbol{u}^{\{r\}}(\boldsymbol{x}, t)\, \mathrm{d}t. \tag{7}$$

To this end, we build R statistical independent realizations of the same flow initialized from different random fields, which are simulated independently in parallel, with an interval for time averaging that is now reduced to T_s/R. For each test case listed above, we construct an ensemble with $R = 4$ members and each member is run on $p = 156$ processors. Thus, for each case in Table I, $pR = 624$ processors are employed in total. This configuration allows an overall speed-up of 540.56, with a parallel efficiency of 0.87.[28]

In the simulations, the time step size is fixed to $\delta t = 0.004 D U_J^{-1}$, enabling us to resolve one period of actuation for the highest frequency case (*C4*) with 200 time steps. The initialization of simulations takes $T_i = 16 D U_J^{-1}$. Afterwards we collect the statistics for a time interval of $T_s = 320 D U_J^{-1}$. For instance, for case *C1*, this relates to 20 cycles of actuation during the initial transient T_i, and 400 cycles during the statistical sampling time T_s.

C. Grid assessment

Before analysing the different control cases in detail in Secs. III and IV, we first perform a grid-assessment study. To this end, we first benchmark the baseline case B2 with a well known experimental work from literature.[29] The comparison is limited to the first order statistics as these are less sensitive to initial conditions and Reynolds number, and converge relatively fast to self-similar profiles downstream. In Figure 3 the decay rate for the centerline axial velocity $U_c = \langle u_x \rangle_{r=0}$

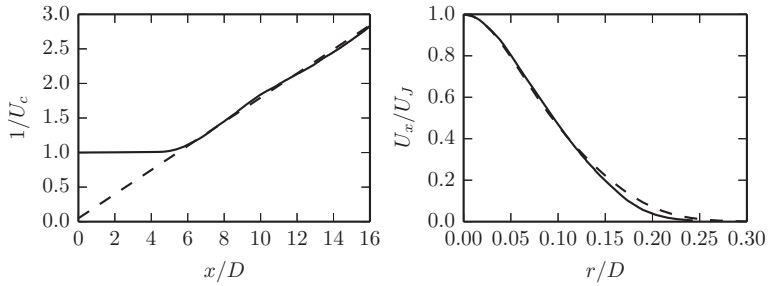

(a) axial velocity (b) turbulent kinetic energy

FIG. 3. Literature benchmark of baseline data. (a) Decay rate for centerline velocity: $U_c = \langle u_x \rangle_{r=0}$. (b) Self-similar profile for axial velocity U_x. (—): case B2; (−−): experimental data in Ref. 29.

and self-similar profile for axial velocity are shown. Numerical results for these quantities are in very good agreement with experimental data except some minor discrepancy for $r/D > 0.15$ in the self-similar profile.

Additionally, we perform a grid sensitivity study. We construct a number of grids for the control case *C1*, and compare statistically averaged results. Two coarser meshes and one finer mesh are constructed, so that we can compare four grid levels, i.e., Level I (coarsest), Level II (intermediate), Level III (original resolution), and Level IV (finest). Details are provided in Table II along with the original case (Level III). On the coarser-grid simulations, we further increased the time step to $\delta t = 0.0064 D U_J^{-1}$ and on Level IV reduced it to $\delta t = 0.0032 D U_J^{-1}$.

In a first step, the evolution of the mass flux $\dot{m}(x)$ and energy flux $\phi_E(x)$ as function of downstream distance x is investigated. These are also used in further sections, and are respectively defined as

$$\dot{m}(x) = \int_0^{2\pi} \int_0^{\infty} \langle u_x \rangle \, r \, \mathrm{d}r \, \mathrm{d}\theta \tag{8}$$

and

$$\phi_E(x) = \int_0^{2\pi} \int_0^{\infty} \frac{1}{2} \langle u_i \rangle \langle u_i \rangle \langle u_x \rangle \, r \, \mathrm{d}r \, \mathrm{d}\theta, \tag{9}$$

and where we numerically evaluate the inner integral up to $8D$ in practice (instead of ∞).

In Figure 4(a) the normalized mass entrainment by the jet, $\dot{m}(x)/\dot{m}(0)$, is shown for the different grid resolutions. It is appreciated that the entrainment is well predicted on all grid levels. In particular results of the intermediate, original, and finest grid level collapse, except for some small differences at the end of the simulation domain for $x > 10D$. In Figure 4(b) the normalized energy flux $\phi_E(x)/\phi_E(0)$ is shown, with also a very good collapse of results for all grid levels.

We now turn to some flow properties that do not benefit form any form of plane averaging (unlike Eqs. (8) or (9)). First of all, in Figure 5(a) the evolution of the centreline axial velocity $U_c = \langle u_x \rangle_{r=0}$ is shown for the different grid levels. We observe that grid convergence for this property is more challenging. In particular results on the coarsest grid differ considerably. The

TABLE II. Employed grids for sensitivity studies. Level III is the original grid used in Secs. III and IV.

Grids	Core region resolution	O-Grid resolution	Total number of elements
Level I	$78(x) \times 78(y) \times 285(z)$	$282(r) \times 312(\theta) \times 285(z)$	26 809 380
Level II	$104(x) \times 104(y) \times 380(z)$	$376(r) \times 416(\theta) \times 380(z)$	63 548 160
Level III	$130(x) \times 130(y) \times 475(z)$	$470(r) \times 520(\theta) \times 475(z)$	124 117 500
Level IV	$156(x) \times 156(y) \times 570(z)$	$564(r) \times 614(\theta) \times 570(z)$	214 475 040

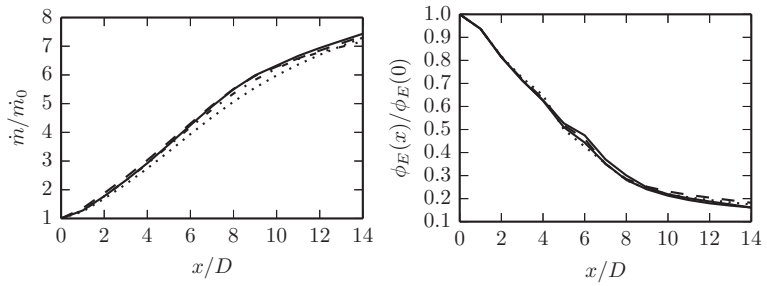

(a) entrainment (b) kinetic energy flux

FIG. 4. Grid sensitivity of planar data. (a) Entrainment rate using vol. flux in Eq. (8). (b) Mean kinetic energy flux in Eq. (9). (· · ·): Level I; (· −): Level II; (—): Level III (original resolution); (−−): Level IV.

intermediate and original grids yield collapsing centerline velocities up to $x = 10D$; beyond that, some differences also occur. The two finest levels have the best agreement as their centerline velocities nicely collapse except for some minor differences in the region $7D < x < 9D$.

Finally, we look at second-order statistics along the centerline of the jet in Figure 5(b), i.e., the evolution of the centerline turbulent kinetic energy $k_c = 0.5\langle u_i' u_i' \rangle_{r=0}$ (with $u_i' = u_i - \langle u_i \rangle$). It is seen that results for the original grid have a very good collapse with the ones of the finest case up to $x = 6D$. Beyond that, significant differences occur. Thus for this last property, grid convergence could not be ascertained for $x > 6D$. Therefore we will limit the discussions on second order statistics to a smaller domain with a length of $6D$. We further investigated the grid convergence of the second-order statistics in this smaller domain by looking at the turbulent kinetic energy contours on transverse planes (not shown here), and found that up to $6D$ the results on the original and reference grid are practically indistinguishable.

III. FLOW DYNAMICS

In this section, we investigate the transitional flow dynamics of the different cases by looking at instantaneous vortex patterns in Sec. III A, and the mechanisms driving their evolution in Sec. III B.

A. Unsteady flow behavior

We present the dominant unsteady flow features playing a crucial role in the momentum and scalar transport. To this end, we visualize isocontours of vorticity modulus $|\boldsymbol{\omega}|$ and isosurfaces of the Q criterion,[30] where Q is the second invariant of the velocity gradient tensor, defined as

$$Q = \frac{1}{2}\left[\Omega_{ij}\Omega_{ij} - S_{ij}S_{ij}\right], \tag{10}$$

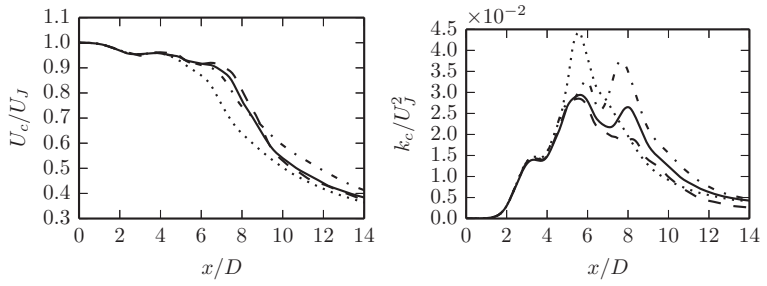

(a) axial velocity (b) turbulent kinetic energy

FIG. 5. Grid sensitivity of examples of flow data along the centreline. (a) Mean axial velocity: $U_c = \langle u_x \rangle_{r=0}$. (b) Mean turbulent kinetic energy: $k_c = 0.5\langle u_i' u_i' \rangle_{r=0}$. See Fig. 4 for captions.

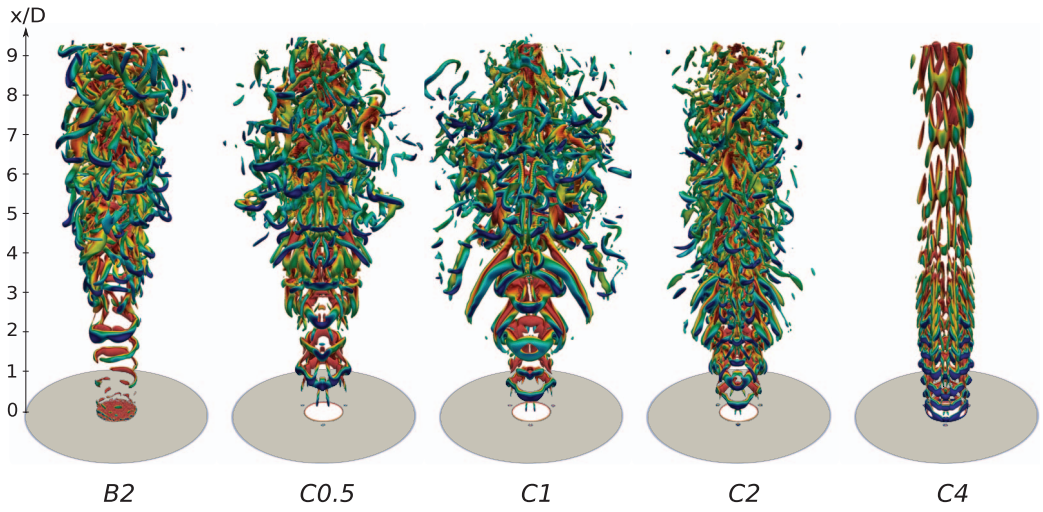

FIG. 6. Visualization of vortical structures by isosurfaces of $Q/(U_J^2/D^2) = 3.267$ (0.3267 for *C4*). Color coded by velocity modulus (maximum value is $0.8U_J$ and coded in red).

with $\Omega_{ij} = [\partial u_i/\partial x_j - \partial u_j/\partial x_i]/2$ the skew-symmetric rate-of-rotation tensor and $S_{ij} = [\partial u_i/\partial x_j + \partial u_j/\partial x_i]/2$ the symmetric rate-of-strain tensor.

In Figure 6 isosurfaces of Q are illustrated. For the baseline case *B2* the single-helix mode is observed in the transition region. In contrast, actuation synchronizes the axisymmetric mode, and a train of strong vortex rings are shed with the actuation frequency. In addition to primary vortices, secondary counter-rotating vortex pairs are also present, located in the braid regions between successive vortex rings. Due to their prominent size and strength these primary and secondary structures are most noticeable in Case *C1*.

Figure 7 presents streamwise snapshots of $|\boldsymbol{\omega}|$ in an actuation plane, i.e., a cutplane passing through the centreline of an actuator (plane given by $z = 0$ in this case, cf. Fig. 1). Jet actuation causes significant changes in these planes as seen in Figures 7(c)–7(f). We see again that in-phase actuation leads to strong formation of vortex rings with round cores that are synchronized to the actuation frequency. A fully grown ring is marked in Case *C1* (cf. red dashed line in Fig. 7(d)). The vortex ring is clearly asymmetric with lower (trough) part on the actuation side ($y > 0$) and higher (peak) part on the other off-actuation side. A three-dimensional view of this asymmetric ring is given in Figure 8. The ring has been distorted azimuthally and longitudinally and has a corrugated pattern. Similar vortex patterns are also seen in experiments with corrugated nozzles[16] or simulations with combined axial and azimuthal forcing.[22]

Looking further at the actuation planes in Figure 7, we note the presence of streamwise vortex filaments in the braid regions. These secondary structures are first formed between the peak sides of primary rings, similar to earlier observations.[10,22] An example is marked for Case *C1* between two fully formed vortex rings using the red solid line in Fig. 7(d). Once these streamwise filaments appear, they free themselves from their trailing vortex rings and spread away from the jet core with large angles to jet axis (cf. blue arrow). We also observe the formation of streamwise filaments and their lateral ejections on the trough sides of the rings, starting from the downstream vortex ring (cf. green arrow).

We first further focus on Case *C1* in Figure 9(b), presenting snapshots of $|\boldsymbol{\omega}|$ on various transverse planes at the same time instance as Fig. 7(d). In general, the actuation causes a profound distortion on the jet cross-section and induces strong anisotropy. The $x/D = 2.3$ plane cuts the first developed vortex ring through the peaks (cf. I in zoom A in Figure 9(b)). The ring has intensive vorticity on peak sides (indicated with P, in zoom A). In addition, we see the formation of counter-rotating streamwise vortex pairs attached to peak sides (cf. II in zoom A). In the braid region, here at $x/D = 3$, these secondary structures grow stronger (cf. III in zoom B). Three initial side jets (cf. IV in zoom B for an instance) are formed which are produced by the motions of counter-rotating

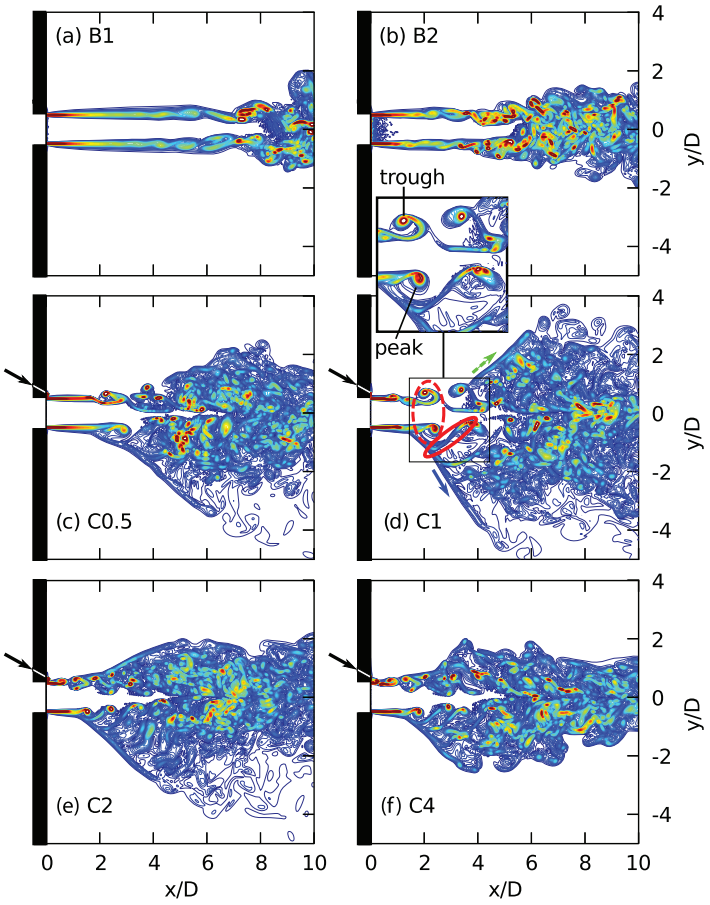

FIG. 7. Snapshots of $|\boldsymbol{\omega}|$ on an actuation plane ($z = 0$).

streamwise filaments (cf. further discussion in Sec. III B). Further downstream ($x/D = 5$), the main corrugated vortex ring deforms and increases its three-dimensionality. New streamwise structures are induced at the trough sides. These new secondary structures produce additional side jets (cf. green arrows) and together with the initial ones (cf. blue arrows) they deform the system into a hexagram, which eventually ($x/D = 7$, 10) disintegrates into finer scales.

We now return to the other actuation cases. For the cases with low frequency actuation, i.e., *C0.5* and *C1*, the vortex rings are well separated from each other and their interaction is limited (cf.

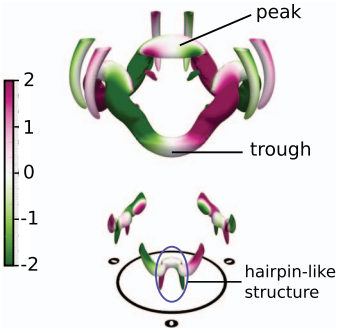

FIG. 8. Initial jet development for *C1* by isosurfaces of $Q/(U_J^2/D^2) = 10.89$. Color coded by helicity density $H' = (\boldsymbol{\omega} \cdot \boldsymbol{u})/(U_J^2/D)$. Secondary vortex features have been removed for clarity of presentation.

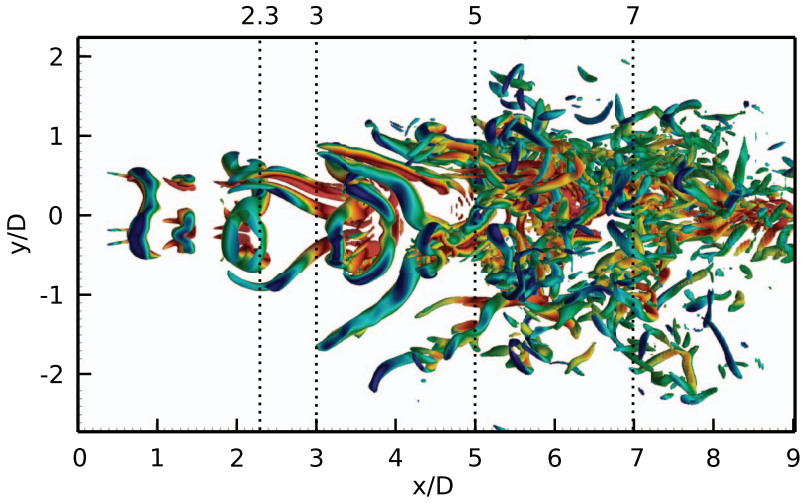

(a) Side view of Case *C1* from Fig. 6.

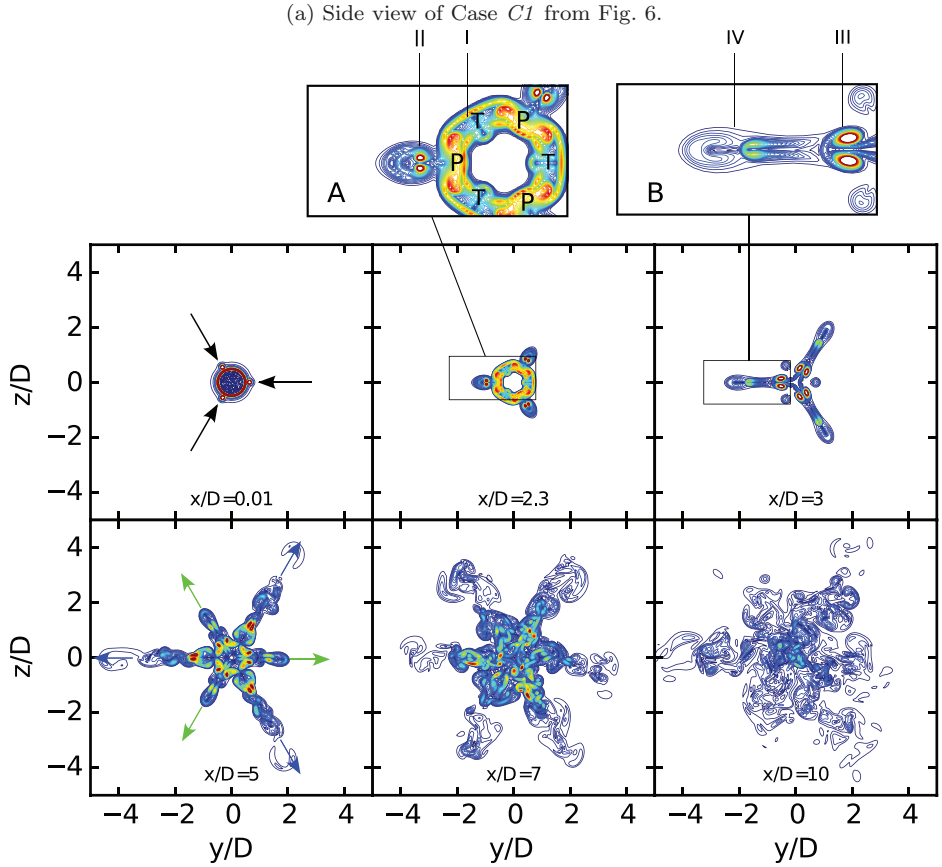

(b) Snapshots of $|\omega|$ on transverse planes. Black arrows: actuation directions; blue arrows: side jets emaneted from peak sides of the vortex rings; green arrows: side jets ejected at trough sides.

FIG. 9. Detailed visualizations for Case *C1*.

Fig. 6). For Case *C2* we noted (not shown here) strong interaction and merging of vortical structures in the potential core. For the high frequency Case *C4*, vortices have substantially smaller size and strength and jet spreading appears to be suppressed.

To further elaborate these observations we present in Figure 10 power spectra of the streamwise component of fluctuating velocity signals at five downstream locations on the jet centerline

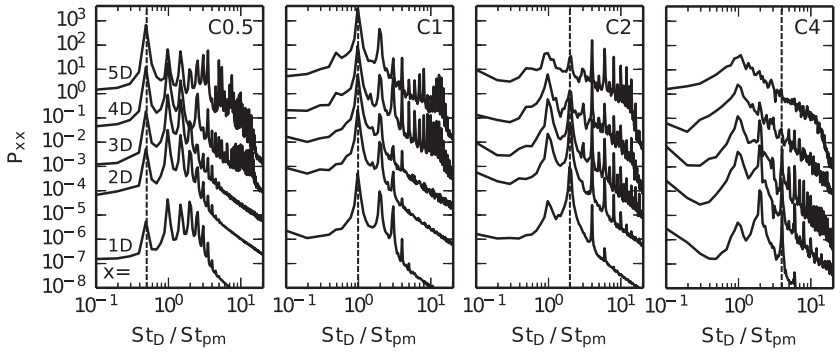

FIG. 10. Power spectra of centreline velocity signals. Each spectrum is shifted one decade starting from the signals on $x/D = 5$. Dashed lines show actuation frequencies.

($r/D = 0$). For Cases *C0.5* and *C1*, significant energy is contained at the actuation frequency until the most downstream measurement point ($x = 5D$). This is not the case for higher control frequencies. Already at $x = 1D$ the presence of subharmonics with increased energy content is clear. Further downstream these subharmonics gain more energy related to the vortex merging mechanisms observed in these cases. At $x = 5$, spectral peaks are hardly noticeable for Cases *C2* and *C4* hinting at earlier breaking-up to small scales.

B. Vortex dynamics

In Sec. III A it was observed that ZNMF controlled jets show distinct departure from axisymmetry. In this section, we investigate the mechanisms leading to the observed topological features.

ZNMF actuation produces isolated mini-vortex rings that are periodically travelling towards the main jet. These mini-vortex rings subsequently impact and distort the jet shear layer. Following this nonlinear interaction, the mini-vortex rings are stretched in streamwise direction by the main jet, and evolve into hairpin-like structures attached to small azimuthal vortex filaments that are the result of the local bending of the jet shear layer in these regions (cf. Fig. 8).

The actuation frequency plays a key role in the evolution of these initial vortex fragments. If the jet is excited with the natural mode, i.e., Case *C1*, then the time and spacing between two consecutive penetration events are long and hairpin-like structures disappear while azimuthal vortex filaments grow. They connect to the KH roll-ups on the unperturbed azimuthal sides, and build corrugated vortex rings. The further downstream development of the jet in this case is very similar to axisymmetric jets subject to periodic azimuthal perturbations[22,23] where strong corrugated vortex rings also emerge and give rise to powerful secondary structures which produce side jets. These side jets remarkably alter the global characteristics of the jet.

In contrast, if the jet is actuated with a high frequency, as in Case *C4*, hairpin vortices interact with each other and inhibit azimuthal structure growth. This mechanism leads to suppression of large scale vortex development and reduces jet spreading. The vortex dynamics for these two distinct cases, i.e., Case *C1* and Case *C4,* are now discussed in more detailed.

1. Case C1: Strong primary structures and side jets

The jet development for Case *C*1 is mainly dominated by downstream evolution of ZNMF induced azimuthal perturbations of the jet shear layer which gradually develop strong primary and secondary large scale vortices. Our discussion is based on vortex induction arguments, inspired by previous numerical studies on inviscid[23] and viscous[22] azimuthally perturbed jet flows in a temporal framework. We show that the downstream evolution of primary vortex structures is characterized by a sequence of self induction, mutual induction with secondary structures, followed by self induction again. The evolution of secondary counter-rotating streamwise structure is initially determined by

mutual induction with the primary structures, followed by self induction. The latter leads to strong side jets that enhance jet spreading and lead to the above-discussed hexagrammoid structure.

To explain these features, we base our discussion on Figures 11 and 12. The first figure shows the primary and secondary vortices in side view, and shows streamwise vorticity in transverse jet sections at different downstream locations. For the sake of discussion, three successive primary vortex rings, i.e., *VR1*, *VR2*, and *VR3*, are marked in the figure. Secondary structures, i.e., counter-rotating streamwise vortex pairs that are formed between the peak sides of the primary rings, are marked with *PP1*, *PP2*, and *PP3* in the figure. The second figure, i.e., Figure 12, shows a detailed zoom on the initial dynamics of a primary vortex ring over the first actuation period $t \in [0, T]$ following its emergence. In order to better represent three-dimensional deformations of the vortex structures in both figures, the helicity density $H = \boldsymbol{\omega} \cdot \boldsymbol{u}$ is used to color Q isosurfaces (e.g., $H = 0$ for an azimuthally unperturbed vortex ring).

We now first turn to the discussion of primary vortex evolution. To that end, we look at Figure 12, and at the vortex regions in Figure 11(c) (i.e., see parts ii and iv). Note that the third sequence in Figure 12, i.e., at $t = 3T/4$ approximately corresponds to the location of the transverse section in part ii of Figure 11(c). At time $t = 0$ in Figure 12 we show an initial wavy vortex ring with an azimuthal wavenumber $m = 3$ that just emerged from three azimuthal vortex segments indicated in Figure 8. The waviness of the ring grows due to self-induced velocities and further deforms the vortex ring at later stages, i.e., $t = T/4$ and $t = T/2$. After that, the effect of self-induction is inhibited, because of the interaction with secondary streamwise structures.[31] This is best seen in part ii of Figure 11(c) (cf. also the zoom A), showing that the strong streamwise vorticity created in the peak regions of the vortex ring is now coupled to an opposite pair of counter-rotating secondary vortex structures. Because of this mutual interaction between primary and secondary structures, the peaks and troughs in the primary vortex ring flatten, as seen by the helicity coloring in Figure 12 for $t = 3T/4$ and $t = T$ and *VR1* in Fig. 11(b). When continuing downstream to the next vortex ring *VR2*, we see that the secondary structures are detached from the primary vortex ring (reasons are further discussed below). As a result, self-induced velocities (indicated with arrows in part iv of Figure 11(c)) that result from the alternate arrangement of streamwise vorticity in the peak regions, push these peak regions towards the jet centerline. Consequently, the vortex ring rapidly deforms into a tripod-like three-dimensional structure with legs on the trough sides (cf. *VR3* in Figs. 11(a) and 11(b) and parts v and vi of Fig. 11(c)).

The evolution of the secondary structures is now discussed. They originate from sheets of streamwise vorticity in the braid region that are arranged with alternated signs (cf. part i of Figure 11(c)). This particular vorticity pattern is generated by the effect of global induction:[23] the radial shear layer of the main jet is azimuthally perturbed by the ZNMF actuation, and is convected faster in regions closer to the jet centerline, i.e., at the ZNMF penetration side. This results in streamwise vorticity with alternating signs as seen in Figure 11(c) (part i). This arrangement of streamwise vorticity leads to self-induction as also shown in Figure 11(c) (part i) with arrows. Moreover, similar to the creation of secondary vortex structures in mixing layers,[32,33] it is well documented[23] that the combination of this self-induction with the stretched strain-field in the braid region between the primary vortex peak sides leads to the generation of secondary structures that are attached to the peak sides of the vortex rings (cf. *PP1* in Fig. 11(c)-part iii and Figs. 11(a) and 11(b)). Initially, mutual induction with the primary vortex ring is dominant in the evolution of secondary vortices, as they have an opposite arrangement of streamwise vorticity (cf. Fig. 11(c)-part ii). This difference is directly related to the different way in which streamwise vorticity is generated in the braid region (global induction) and the ring region (by ZNMF impact and self-induced velocities—cf. discussion above).

The secondary streamwise vortex pairs have very strong self-induction in their braid regions (indicated with arrows in Fig. 11(c)-part iii), which eventually overcomes the effect of mutual induction at their tips. Thus, they free themselves from the primary structures and spread in lateral direction (cf. *PP2* in Fig. 11(a)). As a result, the vortex pairs eject high velocity fluid from the jet core to the ambient and produce side jets (cf. zoom B in Fig. 11). At the same time, in the region between vortex pairs, quiescent ambient fluid is entrained into the potential core (cf. also zoom B in Fig. 11).[18]

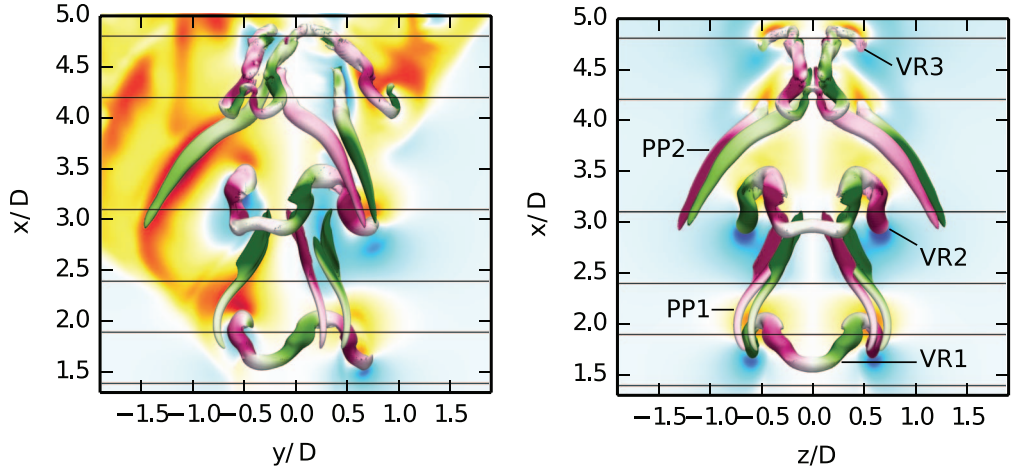

(a) z-view (b) y-view

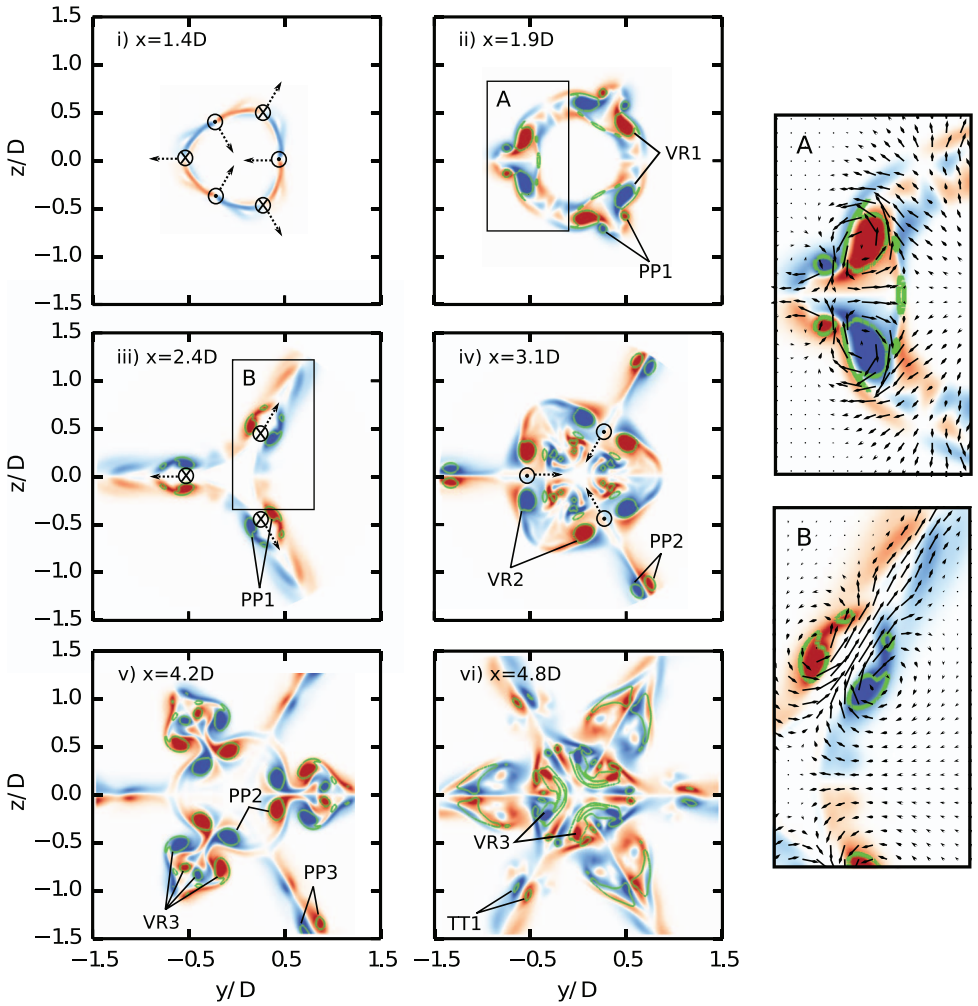

(c) x-views

FIG. 11. Primary and secondary structures in potential core of *C1*. (a)-(b) Side views of 3D isosurfaces of $Q/(U_j^2/D^2) = 10.89$ color coded by normalized helicity density. Only three primary rings and corresponding secondary vortex filaments have been extracted. In (a,b) a streamwise section colored with radial velocity u_r is shown as background; i.e., in (a) the $z = 0$ plane, and in (b) $y = 0$ plane. (c) Transverse sections corresponding to horizontal lines in (a) and (b) visualizing snapshots of streamwise vorticity ω_r and (green) isolines of $Q/(U_j^2/D^2) = 10.89$.

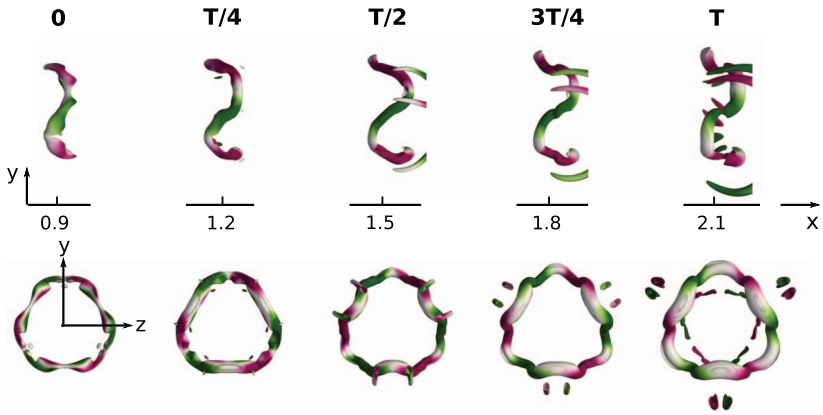

FIG. 12. Temporal evolution of a vortex ring in *C1* by isosurfaces of $Q/(U_j^2/D^2) = 10.89$. Color coded by helicity density. T is one actuation cycle.

Finally, when the primary structure evolves into a tripod-like geometry, self-induced velocities stretches the strain field around the sharp tips in the trough sections, and additional secondary vortex filaments develop (cf. *TT1* in Fig. 11(c)-part vi). The evolution of these newly emerged filaments is similar to the ones on the peak sides. Together with the secondary structures on the peak sides they shape the jet's transverse cross-section into a hexagram.

2. Case C4: Suppression of jet spreading

Now we turn to Case *C4* where hairpin-like structures induced by the synthetic jets play a more dominant role. When the actuation frequency is high, the streamwise spacing between ZNMF induced vortex filaments is low. This has a major impact on the downstream development of the flow as we will discuss in this section. The discussion will be limited to the region close to the orifice ($x < 2$).

To facilitate the discussion, the initial development of Case *C4* is illustrated in Figure 13. The evolution of ZNMF induced mini-vortex rings into streamwise hairpin-like structures is indicated with the sequence *H1–H4* in the figure. It is observed that *H1* is a slightly distorted mini-vortex ring impacting the main jet that generates a small azimuthal vortex filament *A1*. The mini-vortex ring

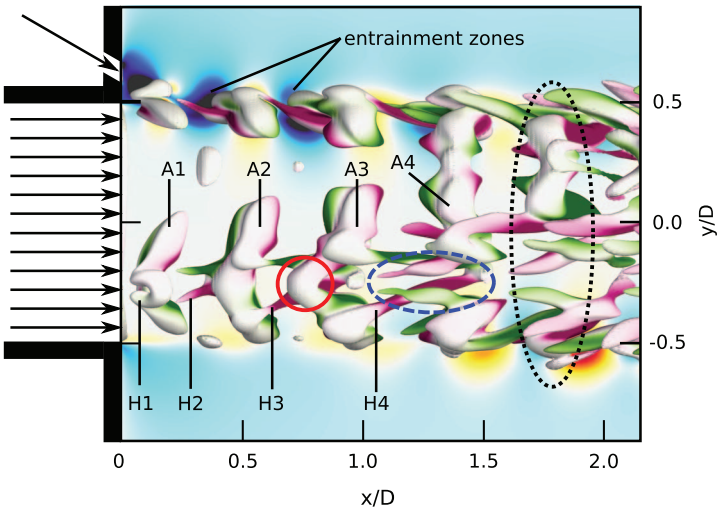

FIG. 13. Initial jet development for *C4* by isosurfaces of $Q/(U_j^2/D^2) = 3.267$. Color coding is the same as in Figures 11(a) and 11(b).

quickly evolves into a streamwise hairpin-like structure that has its head connected to the azimuthal filament, and convects downstream (cf. *A2–H2*). A similar structure is observed in Case *C1* (cf. Fig. 8). The difference in Case *C4* is that now the tails of the hairpin connect to the trailing filament *A1*, and remain more stable.

When looking in more detail at the hairpin vortices *H2* and *H3*, it is observed that they create strong regions of entrainment between their legs (cf. strong negative radial velocity on the other actuation side in Figure 13, i.e., at $y = 0.5$). As a side effect, the nearby azimuthal vortex filaments are pulled into to these entrainment zones, and are strongly deformed (see red circle marking the interaction between *A3* and *H3*). Further downstream, the hairpin-like vortex *H4* largely converts the leading vortex filament *A4* into streamwise vorticity (cf. blue dashed region). This counter-balances the streamwise vorticity of the hairpin itself, inhibiting further entrainment. At this time, the shear layer rolls up at the unperturbed sides into new azimuthal filaments. We believe that this is the result of conventional KH instability. Finally, at the end of the investigated region (cf. region marked with black dotted line), we have small portions of azimuthal KH roll-ups at the unperturbed sides, and a street of streamwise vortices at the perturbed sides of the jets. Remind that in large contrast to this, a strong primary vortex ring has developed in Case *C1* at the same location ($x = 1.8D$) (cf. $t = 3T/4$ in Fig. 12).

The lack of formation of strong coherent vortex rings suggests that large scale primary vortex formation is effectively inhibited by the ZNMF induced hairpin-like streamwise structures in the initial jet region ($x < 2D$) in *C4*. This mechanism substantially delays the growth of conventional primary and secondary structures, suppressing the spreading of the jet (cf. Fig. 6 in Sec. III A). Similar results have been observed in jet control studies with chevron nozzles[34] and steady mini-jets.[11]

IV. MEAN FLOW CHARACTERISTICS

In Sec. III, we saw that different actuation frequencies produce distinctive jet dynamics. Here, we further investigate global jet characteristics using statistical results. Focus is on the common parameters that are often used to describe mixing efficiency, and are either measured on the centerline of the jet (cf. Sec. IV A), or over planes normal to the centerline (cf. Sec. IV B). Next to that, we also present results of scalar transport tubes and flux lines in Sec. IV C. For the discussion of results in this section, it is important to recall that the baseline cases (*B1* and *B2*) have inlet perturbations that are an order of magnitude higher than that of the control cases (cf. Sec. II A), to trigger comparable transition lengths as for the controlled cases (at same levels of perturbations, the baseline cases would remain largely laminar).

A. Centreline statistics

First, averaged results along the jet centerline are presented. Figure 14(a) shows the evolution of the reciprocal of the streamwise velocities $U_c(x) = \langle u_1 \rangle_{r=0}(x)$ along the jet centerline. As may be expected, both baseline cases have a centerline velocity that is approximately constant in the

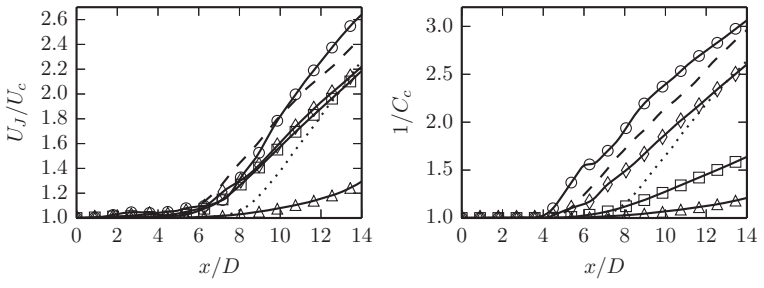

(a) velocity (b) passive scalar

FIG. 14. Evolution of the streamwise velocity $U_c = \langle u_x \rangle_{r=0}$ and the passive scalar $C_c = \langle c \rangle_{r=0}$ along the jet centreline. $(\cdots)$: *B1*; $(--)$: *B2*; (—◇): *C0.5*; (—○): *C1*; (—□): *C2*; (—△): *C4*.

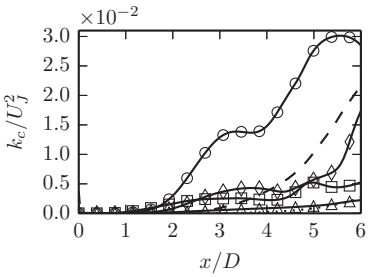

FIG. 15. Evolution of the turbulent kinetic energy $k_c = 0.5\langle u_i' u_i' \rangle_{r=0}$ along the jet centreline. See Fig. 14 for captions.

potential core, then followed by a linear increase of $1/U_c$. Case *B2* has a potential core of $x/D \approx 5$, whereas *B1* has a quite long potential core of $x/D \approx 8$.

Among the controlled cases, Case *C4* clearly illustrates the effect of inhibited jet spreading on the centerline velocity (cf. Figure 14(a)). The potential core is very long, and the subsequent decay rate of the centerline velocity is slow (small slope for $1/U_c$). The transition is a lot slower than that of the baseline cases, resulting from a combination of low jet spreading rate and random perturbations on the inlet that are an order of magnitude lower (cf. Sec. II A). Further, the control cases *C0.5* and *C2* both have a potential core of approximately $x/D = 5$, followed by nearly identical decay rates, with slopes that are slightly smaller than those for the baseline cases. Finally, Case *C1* has the highest decay rate for centreline velocity, and a potential core with the same length as Case *C0.5* and *C2*.

In Figure 14(b) the development of the reciprocal of centreline scalar concentration $C_c = \langle c \rangle_{r=0}$ is shown for all cases. The evolution of C_c is very similar to U_c for Case *C0.5*, *C1,* and the baseline cases. The only difference lays in the slightly higher C_c decay rates compared to U_c. The most noticeable distinction between C_c and U_c evolution is observed in Case *C2*. Here the decay of C_c is very slow in contrast to U_c. Also for Case *C4*, the decay of C_c is a bit slower than that of U_c.

Now we address how the fluctuating part of the velocity is influenced by the actuation in the potential core ($x < 6D$). As a quantitative appraisal for this we check the evolution of turbulent kinetic energy on the jet centreline $k_c = 0.5\langle u_i' u_i' \rangle_{r=0}$. Figure 15 shows k_c normalized using the jet inlet velocity. Among the controlled cases the highest amplification for potential core fluctuations is obtained for Case *C1*. After around $x/D = 2$, Case *C1* shows a rapid increase in k_c, reaching a first peak value of $k_c/U_j^2 \approx 0.03$ at $x/D \approx 5.2$. Case *C4* exhibits a very slow streamwise development of the turbulent kinetic energy, suggesting the efficiency of high frequency actuation to suppress turbulence transition. Among the baseline cases, the *B2* case has a higher turbulent kinetic energy between $4D < x < 6D$ compared to the all controlled cases except *C1*. For Case *B1* the rate of kinetic energy production is comparable to the Case *C4*.

B. Planar statistics

We further address statistics of fluxes through transverse planes, to investigate the global behavior of the jet evolution. First of all, in Figure 16(a) the results for jet entrainment of the ambient fluid defined by Eq. (8) are shown. We observe that the entrainment is enhanced significantly by actuated cases *C0.5*, *C1*, and *C2*. This is mainly due to formation of strong primary vortices and secondary structures which produce side jets. These are known to significantly improve entrainment rates of the jets (cf. discussion in Sec. III B). We observe that actuation of the preferred mode (Case *C1*) delivers the most entrainment to the jet core. This is mainly due to strongest side jet formation for this case. Moreover, we note that high frequency actuation, i.e., Case *C4*, induces a major reduction in entrainment as the growth of large scale structures responsible for entrainment is minimal in this case.

The striking entrainment abilities of controlled jets *C0.5*, *C1*, and *C2* can also be seen in their local entrainment rates, defined as[1] $\kappa = (D/\dot{m}_0)\mathrm{d}\dot{m}/\mathrm{d}x$ presented in Figure 16(b). Close to the jet

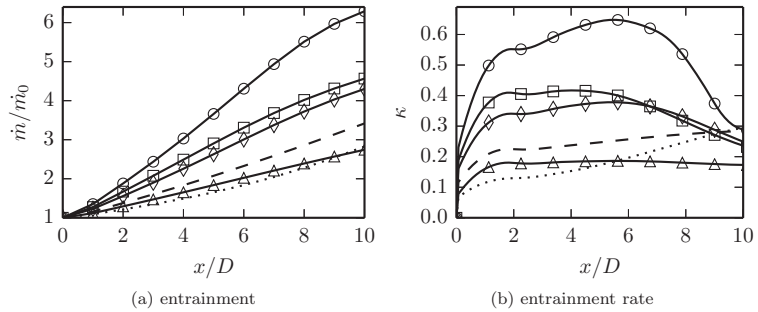

(a) entrainment (b) entrainment rate

FIG. 16. The variation of entrainment and local entrainment rate with axial distance. See Fig. 14 for captions.

origin, the controlled cases (except Case *C4*) exhibit an entrainment rate that grows remarkably faster than the baseline cases. Subsequently ($2 < x/D \approx < 6$) entrainment rates first stagnate for Cases *C0.5*, *C1*, and *C2* and then decrease, dropping back to the levels of the baseline cases.

In Figure 17 the flux of mean kinetic energy (Eq. (9)) along the jet is shown. We see that the initial energy flux decays for all cases. This decrease can be attributed to an increase in the production of turbulent kinetic energy while moving downstream. The highest decay is observed in Case *C1*, showing that this control case is the most efficient in converting mean-flow energy into turbulence.

To further quantify mixing, contours of the mean passive scalar c are shown in a number of transverse planes in Figure 18. Here we see again that initially (around $x/D = 2.5$) the synthetic jets deform the jet column cross-section into triangular-shaped contours. A little bit further downstream $x/D = 5$ we observe the effect of side jets on the transported passive scalar and non-uniform hexagrammoid shapes in the contours are observed. Further downstream the sharp regions of hexagrams entrain fluid and spread, morphing back into triangular-like patterns on the most downstream plots. In order to further visualize the transport of the passive scalar for the different cases, we study the evolution of transport tubes and scalar flux lines next.

C. Scalar transport tubes

In this section, the mixing of the passive scalar is further investigated using scalar transport tubes that are constructed based on flux lines of the scalar transport field. These flux lines are essentially equivalent to the heatlines proposed by Kimura and Bejan,[24] and the related tubes are similar to the concept of momentum and energy transport tubes discussed by Meyers and Meneveau[25] (unfortunately, in Ref. 25, prior reference on heatlines was not included due to authors' unawareness of the literature on heatlines at the time of publication). Here we briefly review these concepts in terms of scalar fluxes, and then apply them to the different jet cases.

First of all, recall that a classical streamline in a stationary mean incompressible flow field is a curve that is constructed tangentially to the mean velocity vector $\langle \boldsymbol{u} \rangle$ of the flow. A classical streamtube is constructed by taking the family of all streamlines passing through a closed curve in the three-dimensional fluid domain.[9] Obviously, by construction, there is no mass transport through

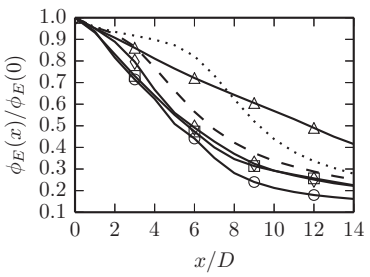

FIG. 17. Flux of mean kinetic energy through transverse planes.

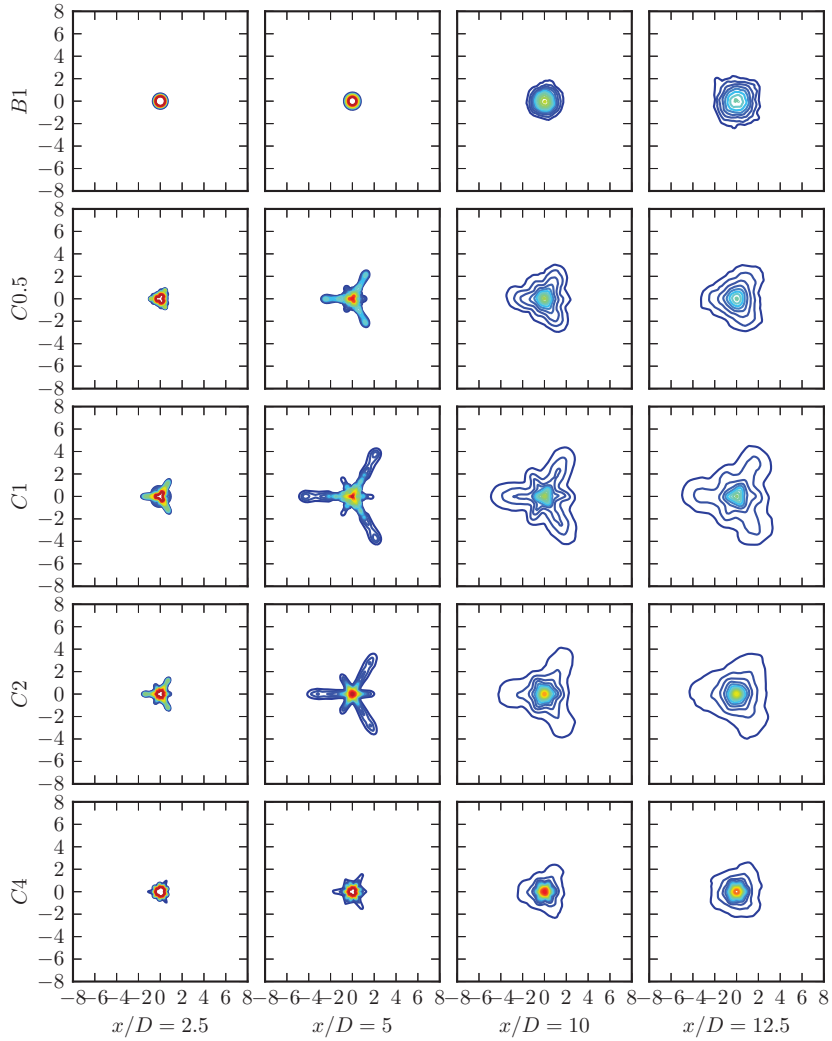

FIG. 18. Contours of mean scalar concentration $\langle c \rangle$ on various transverse planes $x = 2.5D$, $5D$, $10D$, $12.5D$. Contour levels of 0.05 varying between $\langle c \rangle = 0$ and $\langle c \rangle = 1$.

the tube mantle M as $\langle u_i \rangle n_i = 0$ (with n_i the normal vector to the tube mantle). This concept can be extended to passive scalar transport (and other properties)[24,25] by considering the vector field for the Reynolds-averaged total flux of the scalar quantity, i.e.,

$$F_{c,i} = \langle u_i \rangle \langle c \rangle + \left\langle u_i' c' \right\rangle - \frac{1}{Re_D Sc} \frac{\partial \langle c \rangle}{\partial x_i}. \tag{11}$$

Using this flux vector, the Reynolds-averaged scalar-transport equation in a stationary system simplifies to

$$\frac{\partial}{\partial x_i} F_{c,i} = S, \tag{12}$$

where S are potential volume sources of the scalar quantity (here $S = 0$). Thus, if we construct a scalar transport tube based on flux lines along the flux vector field $F_{c,i}$ (and with mantle M, two cross-section A_1 and A_2, and volume Ω), then integration of Eq. (12) over the tube volume and using the Gauss theorem yields

$$\iint_{A_1} F_{c,i} n_i \mathrm{d}\boldsymbol{x} + \iint_{A_2} \mathrm{F_{c,i} n_i d}\boldsymbol{x} = \iiint_{\Omega} \mathrm{S d}\boldsymbol{x}, \tag{13}$$

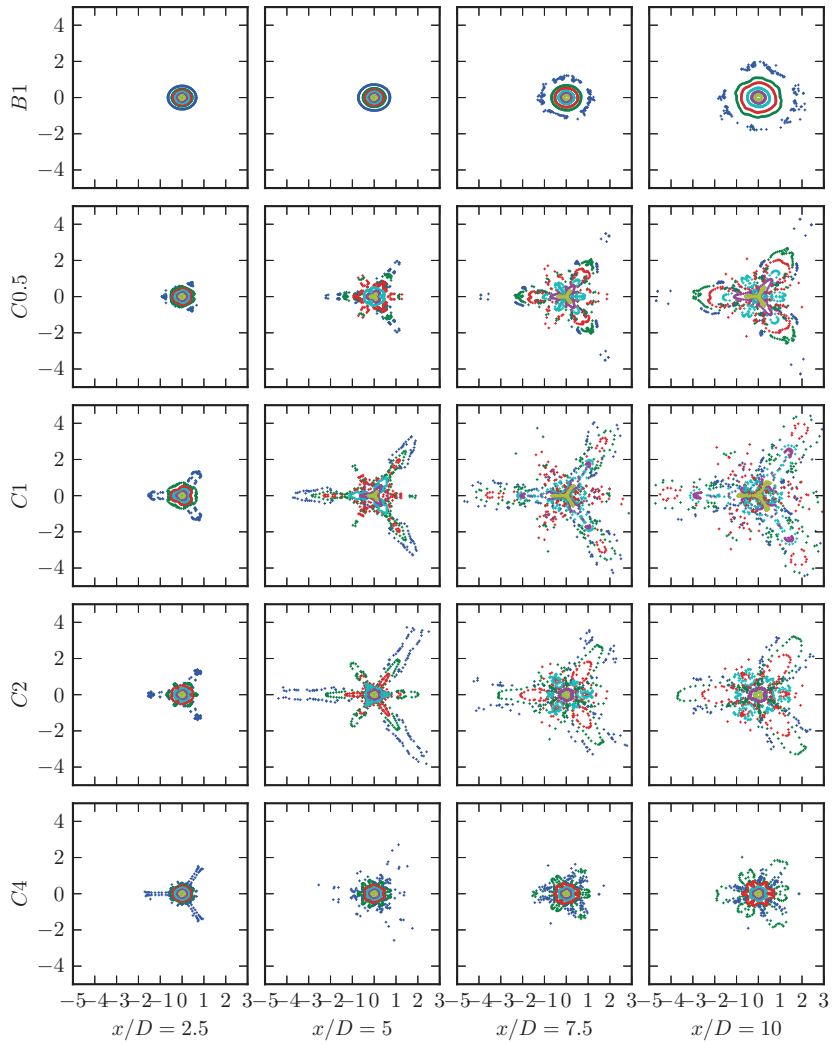

FIG. 19. Transverse sectional views of flux lines starting from concentric circles on the inlet $x = 0$ with radial distances of $2r/D = 0.2$ (yellow), 0.4 (magenta), 0.6 (cyan), 0.8 (red), 0.9 (green), 0.99 (blue). Each circle is seeded with 180 points.

since by construction there are no fluxes over the tube mantle M. Consequently, the constructed tube is a scalar transport tube: i.e., the only changes to the scalar in Ω are due to internal sources S. In absence of sources (as is the case in this work), the scalar flux is conserved along the tube.

In this paper, we use this concept to investigate how the scalar at the jet inlet is transported on average throughout the domain for the different control cases. To that end, a series of concentric circles is selected as starting point for six different transport tubes. Each circle is seeded with 180 points through which flux lines are constructed. In Figure 19 results are presented for the different cases, and the intersection of the different flux lines with planes at $x/D = 2.5$, 5, 7.5, and 10 is shown as points, colored according to the radius of the seed circle from which they originate.

Looking first at the baseline case B1 in Figure 19, we observe that the circular shape of the flux tubes is well conserved downstream—this is quite normal since this case is fully axisymmetric. For the tube starting from the largest circle (colored in blue), we observe that the circular shape is not fully retained for $x/D = 7.5$ and 10, and points are a bit more scattered. This is related to statistical averaging times that are not long enough for this property at these downstream locations: recall that for a round jet, the turbulent time scale is proportional to x^2, so that statistical averages converge considerably slower at large downstream distances.

For the controlled cases in Figure 19, the triangular and hexagonal geometries discussed in Sec. IV B, are recognized again. However there are some distinct differences between Case *C0.5*, Case *C4* (and to a lesser extent Case *C2*) on the one hand, and Case *C1* on the other hand. For the former cases, it is still possible to assemble to the flux tubes at downstream planes (i.e., their intersection with the plane) by connecting points belonging to the same-colored set of flux lines intersects (something we did not do on the figure). For Case *C1* we find that this becomes very difficult, i.e., for the planes $x/D = 7.5$ and 10, the distribution of the flux points has become so irregular that it is impossible to reasonably connect the points and reconstruct the shape of the tube mantle. This may hint at some useful analogies with chaotic mixing for laminar-flow systems,[35,36] and further substantiates that Case *C1* is more efficient in large-scale mixing than the other cases.

V. CONCLUDING REMARKS

In this work we numerically studied a moderate Reynolds number ($Re_D = 2000$) axisymmetric jet subject to multiple miniature ZNMF actuators. The parameters in the study were four different actuation frequencies varying between $St_D = 0.165 - 1.32$. We employed three actuators distributed evenly in circumferential direction and directed towards the main jet with an inclination angle of $\alpha = 30$ to the jet axis. The momentum coefficient of individual actuators is selected to be $C_\mu = 0.0049$. The actuation was implemented as a sinusoidal signal and all the actuators were driven in phase.

All the controlled cases show highly distorted instantaneous shapes and structures, showing the capability of multiple ZNMF actuation in modifying the base jet flow. We clearly observe that the resulting vortices are significantly different from a regular axisymmetric jet. Although the driving momentum coefficient is rather small, the influence on the development of the large coherent structures is significant. The effects are maximal in the case where the actuation is closest to the jet preferred frequency, i.e., Case *C1* with $St_D = 0.33$. In contrast, the evolution of large coherent structures is suppressed by the highest investigated actuation frequency, i.e., Case *C4* with $St_D = 1.32$.

We find that actuation with the preferred mode frequency leads to strong "side jets" that significantly increase the spreading of the jet, and change the geometry of the transverse jet section into hexagrammoid patterns. The mechanisms creating this phenomenon were analyzed, and following scenario was found. First, ZNMF actuation induces azimuthal perturbations on the initial jet profile by penetrating into the jet. As a result, the jet shear layer evolves into strong corrugated vortex rings with peaks at the unperturbed azimuthal locations. These primary structures are shed with the actuation frequency, and are prone to self-deformation. The strain field in the braid regions between the peaks of successive vortex rings is heavily stretched, and as a result, counter-rotating streamwise vortex pairs are formed. As a result of strong self-induction, these secondary structures spread laterally with large angles to the jet axis. This self-induction leads to the production of side jets. These observations are similar to earlier numerical[22] and experimental[18] studies on azimuthally perturbed jets.

We further found that actuation with high frequency, i.e., *C4* with $St_D = 1.32$, prevents above scenario. In this case, ZNMF actuation induces streamwise hairpin-like vortices that play an important role. They break up the azimuthal vortex filaments, and prevent the formation of strong corrugated vortex rings. As a result, jet spreading and mixing are suppressed.

Key characteristics of the jet such as mean entrainment rate, decay rate, and fluctuating energy are also strongly altered following the modifications in the instantaneous motion. First, we observed that the entrainment in the near field is significantly increased when the driving frequency of the controls is close to the natural jet frequencies thanks to the strong side jet production. Similar augmentations have also been observed in other metrics such as centreline decay rate and mean turbulent kinetic energy production. Moreover, we observed that passive scalar transport is enhanced as well by analysing the corresponding transport tubes. The effects on global jet characteristics were completely opposite in the high frequency actuation Case *C4*. In this case, all the characteristic metrics had much lower values and remained even below the reference baseline cases.

In conclusion, the results mark the versatility of ZNMF actuators by showing their effectiveness to promote or suppress turbulence in axisymmetric jet flows. Obviously the considered Reynolds

number is low compared to many practical applications, and, e.g. mixing properties of turbulent jets are known to be Reynolds-number dependent.[37] Nevertheless, we have shown that the mechanisms creating strong side jets are mainly inviscid, and therefore only a weak Reynolds number dependence is to be expected. Indeed, it is well appreciated in experiments with low-density jets that side jet formation occurs for intermediate Reynolds number up to approximately $Re = 25\,000$.[15] For very high Reynolds numbers the noise amplifier nature of the jet becomes extremely dominant, and the growth of strong primary rings is inhibited as the jet becomes very sensitive to unorganized perturbations. Thus, our results remain only relevant for Reynolds number regimes where the formation of strong azimuthal rings can be achieved. Exploring these Reynolds-number regimes in more detail, e.g., using large eddy simulations, is an interesting subject of further study.

ACKNOWLEDGMENTS

The authors acknowledge financial support by the KU Leuven research council (BOF, special research fund, Grant No. OT/08/029). Simulations were performed on the Tier1 computing infrastructure of the VSC Flemish Supercomputer Center, funded by the Hercules Foundation and the Flemish Government.

[1] G. Nathan, J. Mi, Z. Alwahabi, G. Newbold, and D. Nobes, "Impacts of a jet's exit flow pattern on mixing and combustion performance," Prog. Energy Combust. Sci. **32**, 496–538 (2006).
[2] J. Kim and H. Choi, "Large eddy simulation of a circular jet: Effect of inflow conditions on the near field," J. Fluid Mech. **620**, 383–411 (2009).
[3] W. C. Reynolds, D. E. Parekh, P. J. D. Juvet, and M. J. D. Lee, "Bifurcating and blooming jets," Annu. Rev. Fluid Mech. **35**, 295–315 (2003).
[4] C. Winant and F. Browand, "Vortex pairing: The mechanism of turbulent mixing-layer growth at moderate Reynolds number," J. Fluid Mech. **63**, 237–255 (1974).
[5] D. Violato and F. Scarano, "Three-dimensional evolution of flow structures in transitional circular and chevron jets," Phys. Fluids **23**, 124104 (2011).
[6] F. F. Grinstein, "Vortex dynamics and entrainment in rectangular free jets," J. Fluid Mech. **437**, 69–101 (2001).
[7] K. Zaman, M. Reeder, and M. Samimy, "Control of an axisymmetric jet using vortex generators," Phys. Fluids **6**, 778 (1994).
[8] I. Nastase and A. Meslem, "Vortex dynamics and mass entrainment in turbulent lobed jets with and without lobe deflection angles," Exp. Fluids **48**, 693–714 (2010).
[9] G. K. Batchelor, *An Introduction to Fluid Dynamics* (Cambridge University Press, 2000).
[10] D. Liepmann and M. Gharib, "The role of streamwise vorticity in the near-field entrainment of round jets," J. Fluid Mech. **245**, 643–668 (1992).
[11] V. Arakeri, A. Krothapalli, V. Siddavaram, M. Alkislar, and L. Lourenco, "On the use of microjets to suppress turbulence in a Mach 0.9 axisymmetric jet," J. Fluid Mech. **490**, 75–98 (2003).
[12] S. C. Crow and F. H. Champagne, "Orderly structure in jet turbulence," J. Fluid Mech. **48**, 547–591 (1971).
[13] C.-M. Ho and P. Huerre, "Perturbed free shear layers," Annu. Rev. Fluid Mech. **16**, 365–422 (1984).
[14] R. E. Drubka and H. M. Nagib, "Instabilities in near field of turbulent jets and their dependence on initial conditions and Reynolds number," Technical Report AFOSR-TR-82-0962, 1981.
[15] P. A. Monkewitz, D. W. Bechert, B. Barsikow, and B. Lehmann, "Self-excited oscillations and mixing in a heated round jet," J. Fluid Mech. **213**, 611–639 (1990).
[16] J. C. Lasheras, A. Lecuona, and P. Rodriguez, "Three-dimensional vorticity dynamics in the near field of coflowing forced jets," in *Vortex Dynamics and Vortex Method, Lectures in Applied Mathematics* (American Mathematical Society, 1991), Vol. 28, pp. 403–422.
[17] P. A. Monkewitz and E. Pfizenmaier, "Mixing by side jetsin strongly forced and self-excited round jets," Phys. Fluids A **3**, 1356–1361 (1991).
[18] D. Demare and F. Baillot, "The role of secondary instabilities in the stabilization of a nonpremixed lifted jet flame," Phys. Fluids **13**, 2662–2670 (2001).
[19] A. Glezer and M. Amitay, "Synthetic jets," Annu. Rev. Fluid Mech. **34**, 503–529 (2002).
[20] L. G. Pack and A. Seifert, "Periodic excitation for jet vectoring and enhanced spreading," J. Aircr. **38**, 486–495 (2001).
[21] D. A. Tamburello and M. Amitay, "Active control of a free jet using a synthetic jet," Int. J. Heat Fluid Flow **29**, 967–984 (2008).
[22] P. Brancher, J. Chomaz, and P. Huerre, "Direct numerical simulations of round jets: Vortex induction and side jets," Phys. Fluids **6**, 1768–1774 (1994).
[23] J. E. Martin and E. Meiburg, "Numerical investigation of three-dimensionally evolving jets subject to axisymmetric and azimuthal perturbations," J. Fluid Mech. **230**, 271–318 (1991).
[24] S. Kimura and A. Bejan, "The 'heatline' visualization of convective heat transfer," J. Heat Transfer **105**, 916–919 (1983).
[25] J. Meyers and C. Meneveau, "Flow visualization using momentum and energy transport tubes and applications to turbulent flow in wind farms," J. Fluid Mech. **715**, 335–358 (2013).
[26] H. G. Weller, G. Tabor, H. Jasak, and C. Fureby, "A tensorial approach to computational continuum mechanics using object-oriented techniques," Comput. Phys. **12**, 620–631 (1998).

[27] J. van Kan, "A second-order accurate pressure correction scheme for viscous incompressible flow," SIAM J. Sci. Stat. Comput. **7**, 870–891 (1986).
[28] A. Önder and J. Meyers, "HPC realization of a controlled turbulent round jet using OpenFOAM," preprint arXiv:1406.7231 (2014).
[29] H. J. Hussein, S. P. Capp, and W. K. George, "Velocity measurements in a high-Reynolds-number, momentum-conserving, axisymmetric, turbulent jet," J. Fluid Mech. **258**, 31–75 (1994).
[30] J. C. R. Hunt, A. A. Wray, and P. Moin, "Eddies, stream, and convergence zones in turbulent flows," Center for Turbulence Research Report CTR-S88, pp. 193–208, 1988.
[31] F. F. Grinstein and C. DeVore, "Dynamics of coherent structures and transition to turbulence in free square jets," Phys. Fluids **8**, 1237–1251 (1996).
[32] S. Lin and G. Corcos, "The mixing layer: Deterministic models of a turbulent flow. part 3. the effect of plane strain on the dynamics of streamwise vortices," J. Fluid Mech. **141**, 139–178 (1984).
[33] J. C. Neu, "The dynamics of stretched vortices," J. Fluid Mech. **143**, 253–276 (1984).
[34] D. Gaitonde and M. Samimy, "Coherent structures in plasma-actuator controlled supersonic jets: Axisymmetric and mixed azimuthal modes," Phys. Fluids **23**, 095104 (2011).
[35] H. Aref, "Stirring by chaotic advection," J. Fluid Mech. **143**, 1–21 (1984).
[36] J. M. Ottino, *The Kinematics of Mixing: Stretching, Chaos, and Transport* (Cambridge University Press, 1994).
[37] P. E. Dimotakis, "The mixing transition in turbulent flows," J. Fluid Mech. **409**, 69–98 (2000).